



UHASSELT



Maastricht University

KNOWLEDGE IN ACTION

Faculty of Medicine and Life Sciences School for Life Sciences

Master of Biomedical Sciences

Master's thesis

Fabrication of free-standing lipid membrane supports using rapid prototyping techniques

Timo Froyen

Thesis presented in fulfillment of the requirements for the degree of Master of Biomedical Sciences, specialization Bioelectronics and Nanotechnology

SUPERVISOR :

Prof. dr. ir. Ronald THOELEN

MENTOR :

De heer Thijs VANDENRYT

Transnational University Limburg is a unique collaboration of two universities in two countries: the University of Hasselt and Maastricht University.



UHASSELT

KNOWLEDGE IN ACTION

www.uhasselt.be
Universiteit Hasselt
Campus Hasselt:
Martelarenlaan 42 | 3500 Hasselt
Campus Diepenbeek:
Agoralaan Gebouw D | 3590 Diepenbeek

2020

2021



Maastricht University

Faculty of Medicine and Life Sciences

School for Life Sciences

Master of Biomedical Sciences

Master's thesis

Fabrication of free-standing lipid membrane supports using rapid prototyping techniques

Timo Froyen

Thesis presented in fulfillment of the requirements for the degree of Master of Biomedical Sciences, specialization Bioelectronics and Nanotechnology

SUPERVISOR :

Prof. dr. ir. Ronald THOELEN

MENTOR :

De heer Thijs VANDENRYT

Fabrication of free-standing lipid membrane supports using rapid prototyping techniques.Froyen T.^{1,2}, Vandenryt T.^{1,2}, Dilissen S.^{1,2,3} and Thoelen R.^{1,2}¹Engineering Materials and Applications, Institute for Materials Research (IMO), Hasselt University, Diepenbeek, Belgium²IMEC vzw – Division IMOMECE, Diepenbeek, Belgium³Biomedical Research institute, Hasselt University, Diepenbeek, Belgium*Running title: *Rapid fabrication of lipid bilayer scaffolding.*

To whom correspondence should be addressed: Ronald Thoelen, Tel: +32 (11) 26 88 29; Email: ronald.thoelen@uhasselt.be

Keywords: lipid bilayer model, 3D printing, SU-8, microtransfer molding, contact lithography**ABSTRACT**

Various *in vitro* lipid bilayer models are created to replicate the cell membrane. Biomimetic lipid bilayers within physiological-relevant conditions are promising tools for biomedical research. Many therapeutic drugs exert their effect on the cell membrane level. Therefore a high-throughput drug screening method could emerge from artificial lipid bilayers. Additionally, cell membrane research will benefit by enabling membrane protein reconstitution and examination of extramembranous biomolecule dynamics. However, the lipid bilayers should be stabilized while retaining a high degree of freedom. The pore-spanning lipid membrane model (PSLM) is a free-standing cell membrane scaffold allowing membrane mobility. This effect is achieved by a pore array in a solid substrate. This study examines the utility of novel, rapid prototyping techniques to replace costly traditional techniques for PSLM scaffolding fabrication. The first technique is a two-step fabrication method, which combines masked-stereolithography (MSLA) 3D-printing with polydimethylsiloxane (PDMS) microtransfer molding into a SU-8 photoresist. The second technique is a simplified form of contact lithography. First, open pores with diameters below 470 μm could not be achieved by MSLA. However, closed pore formation down to 141 μm in diameter still allowed an inverted PDMS replica of 3D printed designs. The PDMS mold's surface was warped and excessively rough. Therefore, pattern transfer into a negative photoresist resulted in pores with diameters around 1 mm. Second, contact

lithography proved to be successful if photoresists were thinly spin-coated. A 3-4 μm layer resulted in high-definition pores around 55 μm . In conclusion, both novel prototyping methods have potential in future microstructure fabrication.

INTRODUCTION

The study of cell membranes can reveal important information about the pathology and treatment of various diseases. Therefore, a physiological-relevant *in vitro* lipid bilayer model would be a powerful tool for predicting future clinical outcomes. This allows characterization of ion channels, measurements of membrane resistance/capacitance, reconstitution of G-coupled protein receptors and monitoring of interfacial macromolecule reactions and exchanges. The cell membrane is an exceedingly complex structure and consists of many biological components. In general, it is a semi-permeable structure, which acts as the boundary between subcellular components and the extracellular matrix. This biological border consists of several components: glycerophospholipids, sphingolipids and sterols (1). An amphipathic arrangement of lipids results in a bimolecular sheet, called the lipid bilayer. Each lipid contains an apolar fatty acid chain and a polar head group. These physical properties are important for the spontaneous self-assembly process of the bilayer sheet. This process is driven by energetically favorable interactions between the hydrophilic head groups and aqueous solutions, while hydrophobic

fatty acid chains tend towards organic solvents. Consequently, lipid tails align themselves by facing each other in the same dimensional plane, while the polar heads are exposed to the aqueous inner- and outer cellular environments (2). Within the bilayer, a large degree of diversity can be found among the lipids in a chemical and compositional sense. The chemical diversity emerges because of various differences of the backbone structure, head group or the number of tails. The compositional differences refers to different ratios of specific lipids in the bilayer. All components and their differences play a major role in the membranous structural integrity, protein scaffolding properties, lipid metabolism and other processes of the lipid physiology. Any improper regulation of the bilayer composition can result in various diseases (3). Additionally, several proteins are embedded in or attached to the cell membrane. Their interaction with the membrane separates them into two main groups: transmembrane proteins and surface-bound membrane proteins. The former group of proteins span their entire structure across the bimolecular sheet with hydrophilic parts protruding both sides of the extramembranous surroundings. The latter protein group has an anchoring-point on the fatty acid chains or the head group via electrostatic interfacial reactions (e.g. Van der Waals forces) (4). The different protein groups within the cell membrane have several functions: receiving, processing, amplifying and sending out information, energy, stimuli, ions and medicine. These embedded proteins are critical for overall cell functioning, cell-cell communication and extra-cellular matrix (ECM)-cell communication (5-7).

This is facilitated by interchange of metabolites, surface-adhesion, ion in- and uptake and receptor-mediated signaling. Passively traversing the bilayer is only possible for small polar or apolar molecules (e.g. water) while macromolecules and larger metabolites require protein transporters (8, 9). The importance of membrane proteins is apparent in several fields of biomedical research: neurodegenerative diseases (e.g. chaperone-mediated autophagy), channelopathy transport diseases (e.g. cystic fibrosis), lipid metabolism disorders (e.g. Tay-sachs disease), bone remodeling deficiencies (e.g. Paget’s disease), autoimmune disorders, proper organ functioning, immunotherapy, drug delivery, and many other pathologies/uses (10-16).

An *in vitro* model, which consists of a lipid bilayer within a biomimetic environment as seen in cells, could provide an experimental setting for pathology discovery and membrane component characterization. In the past, researchers have developed different biomimetic lipid bilayer models with fixed protein structures. The most straight-forward approach is known as the supported lipid bilayer model (SLB), as seen in figure 1. The fabrication involves the placement of lipid bilayers on planar substrates. This can be achieved by either the Langmuir-Blodgett method or via a giant unilamellar vesicles (GUVs) rupture/adherence process (17, 18). The final product consists of a lipid bilayer separated from a planar support by a thin layer (nanometer range) of water (19). This model exhibits great mechanical stability, as the supporting substrate serves a crutch

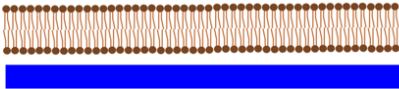
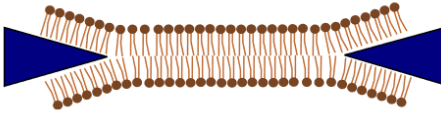
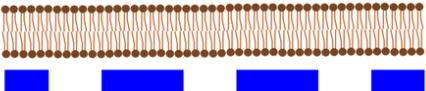
Lipid Model	Advantage	Problem	Figure
Supported lipid bilayers	Stability	Minimal mobility	
Black lipid membrane	Free-standing	Organic solvent	
Pore-spanning lipid membrane	Stability/free-standing	Pore fabrication	

Figure 1: The different cell membrane models. The name, advantages, disadvantages and visual representation of three lipid bilayer support models.

to accommodate the lipid bilayer. This design allows for restricted lateral movement of lipids, but severely limits any motion in the third dimensional plane (20). A high degree of lipid mobility in all directions is an important feature for *in vitro* models. Free movement in the XY-plane facilitates receptor clustering and transport. This spatial reorganization of protein receptors promotes nano- or microscale clusters for various purposes such as amplification (21). Any free movement perpendicular to the XY-plane allows for proper G-coupled protein receptor reconstitution and activity. Therefore, a free-standing lipid bilayer is necessary to replicate a physiological-relevant biomimetic cell membrane. More advanced lipid bilayer models are characterized by this additional feature. The free-standing membrane model consists of a lipid bilayer, which is spanned over a single or multiple apertures. Currently, this design can be categorized in two models (Fig. 1): the black lipid membrane model (BLM) and the pore-spanning lipid membrane model (PSLM). The BLM model is composed of a suspended lipid bilayer that reaches over a single microaperture. The lipid bilayer is not supported by a solid substrate, thus this suspended bimolecular sheet has a free-standing character (22, 23). This membrane divides two compartments in a microfluidic flow cell, which are both individually accessible in order to manipulate the extramembranous environment. The biggest problem with BLM models lies within the fabrication process. This procedure requires the entrapment of an organic solution by aqueous solvents at the aperture border, such that lipids can orient themselves along the interface. However, organic solvents alter lipid diffusion behavior and transmembrane protein function. Heo *et al.* eliminated this problem by suspending the membrane within a polydimethylsiloxane (PDMS) device, because of its intrinsic ability to absorb organic solutions. Despite the complete removal of organic residuals, the reusability of the device becomes unreliable due to PDMS swelling and deformation after repeated cycles of solvent absorption (24). Moreover, the model exhibits some degree of structural instability because the membrane is mostly held together by weak non-covalent interactions between the various lipids. Such interactions can easily be overcome by mechanical and electrical forces (25). This makes the artificial cell membrane fragile and difficult to

work with. To counteract these problems, researchers have developed the second type of free-standing lipid membrane model: the pore-spanning lipid bilayer model. This version could be seen as a combination of the SLB and BLM model. A flat array of pores ranging in the lower micrometer or upper nanometer regime is fabricated with the intent to sufficiently stabilize the membrane, while still granting it a free-standing character. The small pores within the planar substrate maximizes lipid mobility in all directions. The free space facilitated by the grants grants an extra degree of freedom. At the same time, the solid spaces between the pores grant the bilayer overall stability. Lipid painting can be achieved using GUV rupturing/adherence in aqueous solutions, thus no organic solvent is required (26-28). The flat porous support is known as a micro- or nanosieve, depending on the pore size.

The production of sieves containing high-resolution micropores requires specialized technology, capable of producing microstructures with excellent precision. Silicon processing technology methods are a reliable way to fabricate micro- or nanosieves. These methods have resulted in sieves with pore sizes between 0.1-50 μm and exhibit an excellent pore size distribution (29). Silicon micromachining involves well-established techniques like photolithography and precision-etching, which are highly reliable. In silicon photolithography, a thin film of photoresist is spin-coated on top of a silicon wafer. Upon UV-exposure negative photoresists become insoluble, while the reverse applies for their positive counterparts (Fig. 2). By exposing the pre-treated substrate to an UV light source through a photomask, micro- and nanosized patterns can be transferred to the photoresist film. The pattern in the photoresist is obtained by removing all soluble remains. Further, the insoluble photoresist protects the thin film on the substrate from etching procedures with wet chemicals. Stripping of the photoresist residuals from the thin film leaves the desired pattern on the substrate as the end product (30). This method achieves excellent resolution in processing of microchips, biomedical devices, and so forth. However, this technique is expensive, time-consuming, labor-intensive and requires specialized equipment and infrastructure. The production of a new photomask costs several

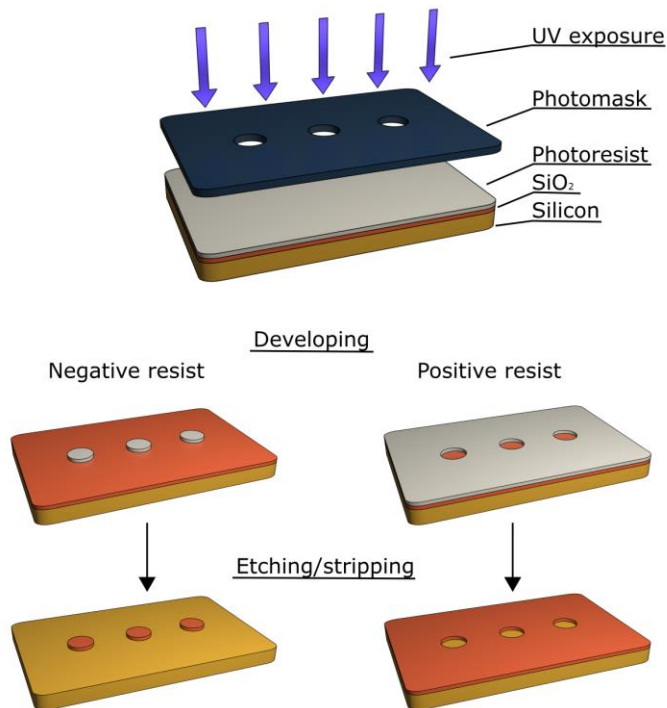


Figure 2: Projection lithography in silicone processing. A photoresist adhered to a SiO₂ thin film is exposed to UV illumination. Negative photoresists become insoluble, while positive resists become soluble during UV exposure. Etching and stripping of SiO₂ is guided by the remaining photoresist on top.

hundreds of dollars, while less expensive masks exhibit poor wearability. The multitude of procedural steps accounts for the long-winded duration of fabrication and the amount of manual labor if the process is not automated. Moreover, researchers require a facility with specialized clean rooms and silicon processing equipment (31). These problems hinder rapid prototyping of biomedical devices by preventing fast reiteration and inexpensive remodeling of any apparatus. In recent years, additive manufacturing has emerged as a means of rapid fabricating of devices. It's already playing an important role in the jewelry, dental, engineering and sports industry.

Currently, 3D printing technologies are being investigated for their potential use in various biomedical fields. First, computer generated models are created using specialized software to create a digital twin of the intended device. A second program slices each model into separate layers. The separation into individual building blocks is necessary because additive manufacturing

commonly operates in increments. This information is stored in computer aided design (CAD) files, which can be read by additive manufacturing machines. In the past, a multitude of microfluidic structures have been created using digital light processing (DLP) or masked-stereolithography (32) (Fig. 3). In general, stereolithography technique solidifies photopolymerizable liquid resin by UV light exposure. The 3D print base solidifies to the building plate, which moves incrementally, vertically upwards after each step. The difference between the two techniques can be found in the mechanism to selectively let UV emission pass through in the XY-plane. The UV light must penetrate the resin in a predetermined pattern to solidify different but compatible layers. The total number of stacked layers ultimately form the final physical object. In order for this to work, the process must be fulfill two requirements: (i) the UV light emission must be spatially controlled, and (ii) each fabricated layer must move up in identical increments in order for new layers to be solidified (33). The DLP approach utilizes a digital mirror device (DMD) to

locally control resin illumination. An UV light source is reflected by the DMD, which is made up by several millions of tiny mirrors. These mirrors can be controlled independently by rotation, therefore defining an exposed pattern in the resin vat (a container with a transparent bottom). The activation of mirrors is directed by the CAD file, such that the pattern of activated mirrors is identical to the solidified layer in the resin vat at that stage (34). In contrast to DLP, the MSLA approach has a more straightforward method. A LED light is projected directly onto a digital LED photomask. The photomask is a LCD panel, which is composed of square pixels and in close proximity to the bottom of the resin vat. Light can pass through individual pixels of the photomask upon deactivation (35). Similar to DLP, the activation/deactivation of individual squares is instructed by the information within CAD files. Because stereolithography can solidify a whole layer at once using two-dimensional patterns of light, fabrication times are significantly reduced compared to other 3D printing technologies (e.g.

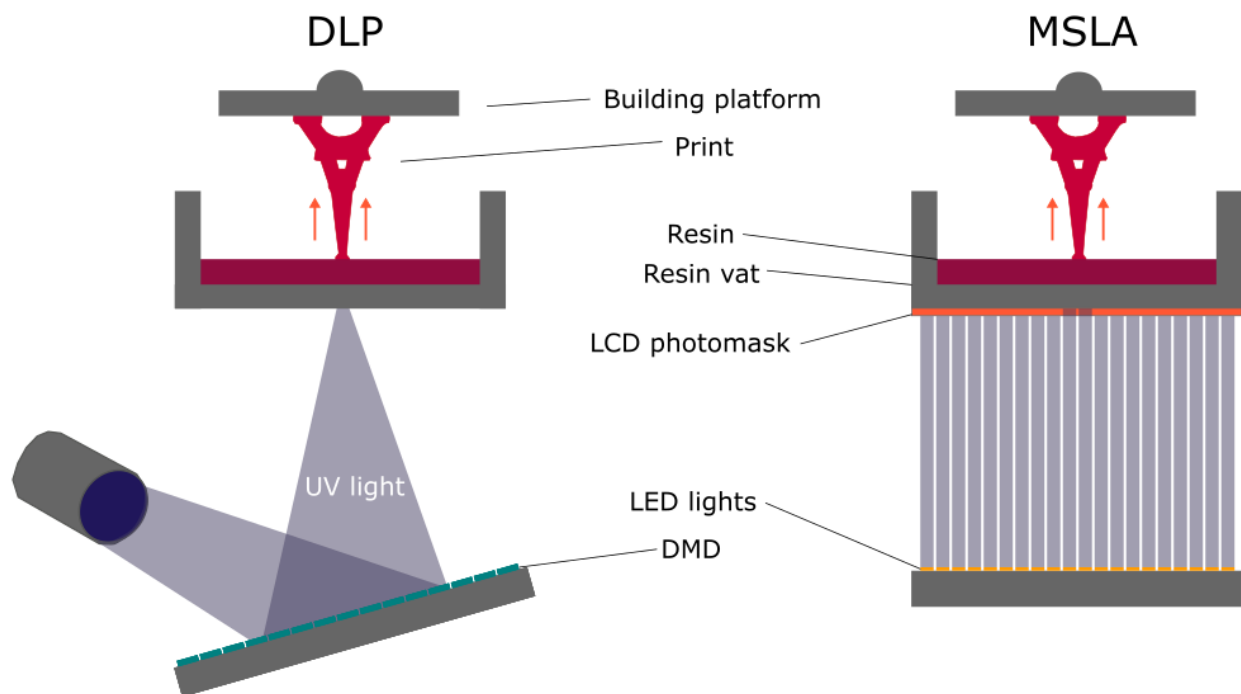


Figure 3: The mechanics behind DLP and MSLA printing. The digital light processing (DLP) technique uses a digital mirror device (DMD). The masked stereolithography (MSLA) method combines a LED array with an LCD photomask.

inkjet, micro-extrusion, laser assisted printing, ...) (36). Both techniques build their models on platforms that are able to automatically move vertically in well-defined steps, to incrementally leave space for the next illuminated resin layer. Stereolithography 3D printing would be an excellent alternative for photolithography because of its low costs, low maintenance and reduced fabrication times (37).

The limited diversity of available materials for device fabrication is a drawback in stereolithography 3D printing. The ideal resin material would have a high resolution, high biocompatibility and great toughness. However, resins possessing all three qualities are lacking in the commercial world. A common non-commercial candidate for printing biomedical devices is poly(ethylene glycol) diacrylate (PEG-DA). This material is biocompatible and photopolymerizable. This material has previously been used for microdevice production due to its functionalization and cell-adhesive properties (38). However, the resolution is limited and currently not able to produce complex features such as pores within the lower micrometer regime. Therefore, the pattern of a non-biocompatible, high-precision resin must be

transferred to a non-cytotoxic material in order to create functional microsieves. The SU-8 negative photoresist is great epoxy-based candidate because of its high patterning resolution, great mechanical strength, chemical stability, biocompatibility and functionalization potential (39). Furthermore, its surface chemistry is able to bind nitrilotriacetic acid (NTA) that can tether his-tagged proteins (40). Such procedures are useful for membrane protein reconstitution and drug delivery analysis purposes. This material has already proven its worth in the fabrication of numerous biomedical microsystems and is commonly processed by photolithography (41).

In this study however, we would like to step away from the traditional lithography procedures due to aforementioned reasons. The combination of 3D printing with soft lithography could pose a solution to this problem. Soft lithography is the collective name of various techniques using elastomeric molds or stamps involving microstructure fabrication and replication. These prototyping techniques are characterized to be rapid, inexpensive and of high-resolution. A single step procedure with an elastomeric mold can fabricate biotechnological structures on a micrometer or

submicrometer scale (42). This concept can be achieved by a technique called microtransfer molding (μ TM). Qian *et al.* achieved 10 nanometer-scaled craters using replica molding with organic polymers (43). The general process for μ TM is simple, inexpensive and quickly achieved. An elastomeric mold containing the negative imprint of the desired microstructures is filled with a liquid prepolymer solution. Mold placement on a planar substrate is necessary before thermally or photochemically solidifying the polymer precursors. This will create a flat microsieve surface with a low degree of surface roughness, depending on the substrate. The elastomeric mold can simply be peeled off, hereby leaving only the hardened polymer behind on the substrate (44). The most popular elastomeric material used for biomedical microfabrication is polydimethylsiloxane (PDMS). Its popularity comes from several characteristics: (i) elastomeric nature, (ii) atomic-level contact for molding, (iii) biocompatibility, (iv) optical transparency, (v) permeable for gases and (vi) adjustable wettability (45, 46).

Another way of rapid prototyping will be investigated aside from combining 3D printing with microtransfer molding. It is already established that silicon processing is a time-consuming, expensive and laborious process. However, lithography remains a well-established, reliable method for microfabrication. A simplified version of photolithography could facilitate a more straightforward for microsieve production. Projection lithography is the most used version in industrial production and biomedical research. Herein, a picture of the photomask is projected onto the sample to achieve great resolution (47). The complexity and cost of the necessary machinery can be drastically reduced by replacing the proximity technique with contact lithography (48). In this approach, a photomask is pressed against the substrate to establish a physical contact during UV exposure. The minimum feature size (MFS) for contact lithography is equal to $\sqrt{d * \lambda}$, where d stands for the thickness of the resist and λ signifies the wavelength during exposure (49). However, it must be noted that this method does come with drawbacks. The mechanical contact between the photomask and the substrate can cause artifacts to both surfaces. Thus, quality of the product can

degrade over time if frequently used (50). Another way to simplify the process is by leaving out the silicone material. Biocompatible photoresists can act as scaffolds which are directly manufactured, thereby leaving out multiple steps out of the traditional procedure. Again, the photoresist SU-8 is a great candidate to serve as the lipid membrane scaffolding material.

In this study, we examine the potential of three-dimensional printing techniques combined with soft lithography for microsieve production in regards to PSLM models. Also, the contact lithography technique will be investigated because simplification of traditional photolithography is greatly advantageous for researchers. The utilization of rapid prototyping techniques to produce microstructures would greatly benefit microsystem productions by excluding traditional photolithography procedures. A functional product would result in rapid cell membrane model fabrication, which can be of great interest in various biomedical fields.

EXPERIMENTAL PROCEDURES

Two-step fabrication method

3D printing - The microsieve (the pore array support) master fabrication was achieved by an Original Prusa SL1 3D printer (Prusa3D). As resin, both Azura Blue Tough resin (Prusa3D) and UV DLP Castable Pink (Photocentric3D) were investigated for microstructure construction. Estimated printing times of both resins were approximately 30 min and 2 h, respectively. Removal of the print from the building platform was followed by cleaning any left-over resin in an agitated isopropanol bath. This latter container was placed in an Original Prusa Curing and Washing Machine (Prusa3D, CW1) for 5 minutes. After rinsing, the model was dried using a nitrogen gun. Second, it was placed in an oven for 1 h at 75 °C. After drying, a final UV exposure treatment was given by the aforementioned CW1 for 5 min. Furthermore, the surface of the microsieve 3D print was coated with a single layer of acryl-based lacquer (Spectrum Paint & Supplies, Clear Varnish) to enhance PDMS curing. After surface-coating, the

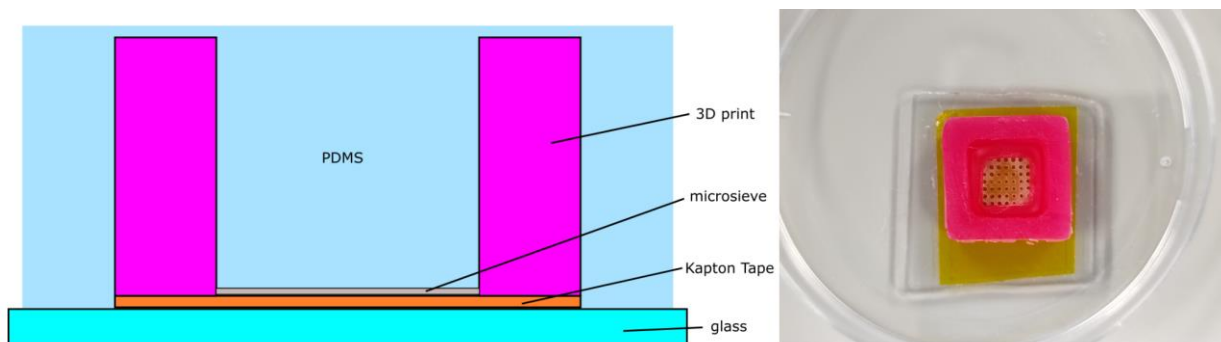


Figure 4: Production of microsieve molds. A microsieve is applied to a glass substrate by double-sided Kapton tape for PDMS curing. A visual representation (left) and a photo (right) indicate how all components are stacked.

model was immediately placed in an oven for 1 h at 75 °C.

CAD modelling -The information input for 3D printing was generated by creating CAD models. All virtual models were designed with the Product Design & Manufacturing software Fusion360 (Autodesk). Additionally, the model was processed with PrusaSlicer-2.3.0+win64 (Prusa3D, Slic3r). As dictated by the latter program, no extra supports were added to the model and layer height was set on 0.01 mm with 10 faded layers. The set exposure and initial exposure times were resin-specific. Azura Tough blue resin required 7 s/ 35 s and Photocentric3D casting resin 20 s/ 120 s, respectively.

Microtransfer molding - A negative PDMS imprint of the microsieve master was necessary for pattern transfer. This inverted pattern will be referred to as pillars. The microsieve 3D print was attached face-downwards to a borosilicate microscope slide (VWR) with double-sided Kapton tape (CapLing) (Fig. 4). A silicone elastomer curing agent (Sylgard 184, Sigma-Aldrich) and a silicone elastomer base (Sylgard 184, Sigma-Aldrich) were mixed in a 1:10 ratio, respectively. Trapped air bubbles were removed by incubating the mixture in a vacuum chamber for half an hour. Subsequently, the microsieve masters were submerged with the silicone blend in a petridish. When placed in an oven at 75 °C, the mixture solidifies overnight into a hardened PDMS elastomer. The PDMS mold can be trimmed to final dimensions with a scalpel blade. If the PDMS cast feels sticky to the touch, the cast will be placed in the oven until fully cured.

The pattern transfer is performed by curing photoresist material inside the PDMS mold (Fig. 5).

First, a glass microscope slide was cleaned with acetone. The PDMS stamp was cleaned with high-purity water (Milli-Q). Both components were dried with cleanroom wipes and a nitrogen gun. A small droplet of SU-8 2005 (Kayaku Advanced Materials, Inc.) was placed in the elastomeric mold with a Pasteur pipet. Excess photoresist material was removed by scraping a knife over the PDMS surface. The photoresist-filled side of the PDMS mold was pressed against the glass microscope slide. Sufficient pressure was applied to avoid any SU-8 remnants underneath PDMS microstructures. Using a heater plate, the complex was warmed for 5 min at 65 °C. Subsequently, the temperature was elevated to 95 °C for half an hour. No exposure or hard-baking steps were required during the procedure. After cooling, the PDMS mold was peeled off the glass slide, thus leaving the hardened SU-8 material behind.

Contact lithography

Photoresist film - A glass microscope slide was cleaned using acetone and dried with cleanroom wipes. The protective foil of a positive photosensitive PCB dry film (Riston Dupont) was peeled off and applied on the glass slide. Heat and compression were generated by a pre-heated hair straightener for 1 min in order to adhere the film onto the substrate surface. For the exposure step, a C.I.F. Mi 10-16 UV-emitter was used containing four Sylvania Blacklight F15W T8 BL 386 lamps, which emit 15 W/cm² each. A copper TEM grid size 200 (Sigma-Aldrich) was used as a photomask during the contact lithography experiments. Physical contact between the dry film and TEM grid was achieved by closing the lid of the emitter, thereby applying pressure on both. The substrate

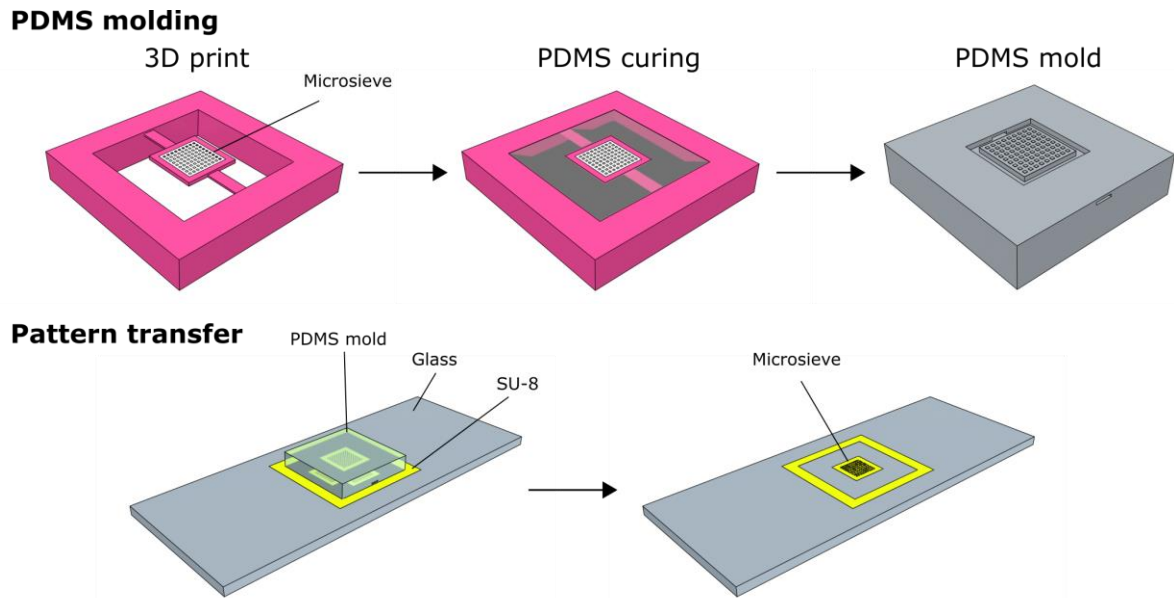


Figure 5: Microtransfer molding a 3D printed microsieve to SU-8 photoresist. *PDMS molding: A 3D printed microsieve is embedded in polydimethylsiloxane (PDMS). The elastomeric material solidifies to a mold by means of crosslinking. Pattern transfer: The mold is filled with a SU-8 photoresist and subsequently pressed against a glass microscope slide. UV illumination will harden the photoresist, thus creating an identical pattern.*

was exposed through the photomask with UV light for 30 s. Next, the second protective foil was peeled off the other side of the dry film. Immediately thereafter, the photoresist was developed in a sodium carbonate solution (4 mg Na₂CO₃ in 250 ml Milli Q) for 2 min.

Thin-coated photoresist - Again, a glass microscope slide was cleaned using acetone and dried with cleanroom wipes. Afterward, a thin layer of SU-8 2005 (Kayaku Advanced Materials, Inc.) was spin-coated onto a glass microscope slide using a SPIN150i spin-coater (POLOS[™]). A few droplets SU-8 were placed on the slide before subjecting it to a thin-coat treatment at 500 rpm/s for 10 s (acceleration: 100 rpm/s) and a consecutive step at 3500 rpm/s for 30 s (acceleration: 300 rpm/s). Next, a soft bake of the photoresist was performed using a heater plate at 95 °C for 2 min. These activated substrates were stored in petridishes wrapped in aluminum foil for maximum three days. Again, the C.I.F. Mi 10-16 UV-emitter was used for exposure steps. This time, a copper TEM grid size 200 and 400 (Sigma-Aldrich) acted as photomasks to investigate the resolution. A post-bake step was performed at 95 °C for 10 min utilizing a heater plate. After the post-bake step, the substrate was developed in SU-8 Developer (Kayaku Advanced

Materials) for 2 minutes, cleaned with IPA, and blow-dried using a nitrogen gun. Lastly, the SU-8 grid is hard-baked at 95°C for 15-30 minutes with the heater plate.

Imaging techniques - The optical microscope Axiovert 40 MAT (Zeiss) with a HAL 100 light source (Zeiss) visualized all microstructures and artifacts within the microsieves. Additionally, the Elyra PS.1 confocal microscope (Zeiss) was used to further analyze all products. Lastly, TEM grid projections in dry film were visualized with an Inskam302 2MP 1000X USB camera.

Surface roughness - The topology of various materials was examined by the stylus profilometer Dektak XTL (Bruker). The obtained data was analyzed with Vision64 MAP 5.51 software (Bruker).

RESULTS & DISCUSSION

Two-step fabrication method

Resin residue contamination –

The production of a high-resolution mold requires a well-defined master print with a clean surface. Any irregularities in the design will be

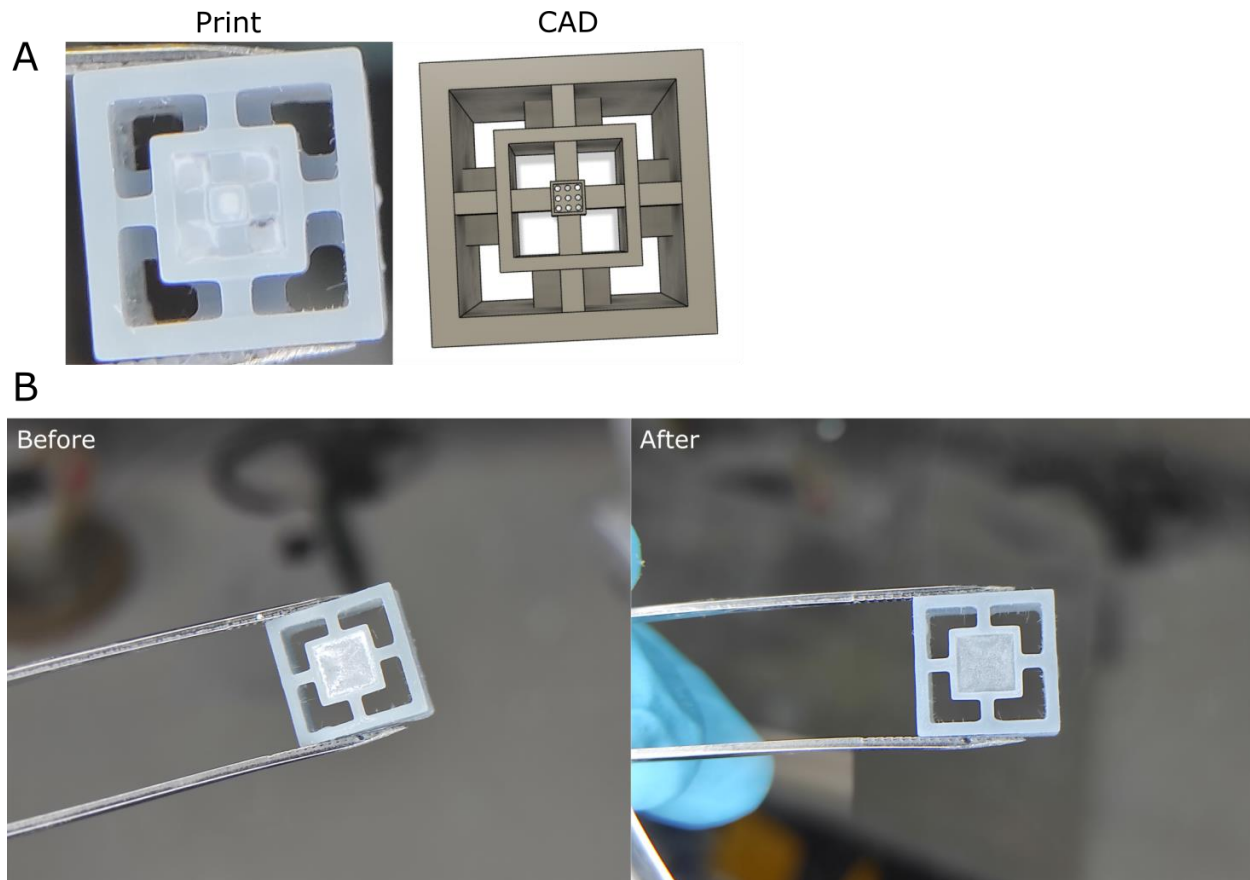


Figure 6: Cleaning of resin print. (A) Residue accumulates mainly in the center. CAD is given of the print.. (B) (Before) The surface of the microsieve is covered by white residue. (After) drying of model and subsequent sonication with IPA and acetone.

transferred to the PDMS stamp during casting. Therefore, the surface of 3D-printed microsieves was inspected before taking further steps in the protocol. A microsieve was designed to contain 200 μm (side length) square pores. This print was produced by illuminating the Prusa Azura Blue resin with UV light. However, the problem with this type of resin was the excessive white residue left on the surface of the print, after cleaning with the prescribed protocol. Printing the design horizontally or vertically had no diminishing effect on the contamination. This powder turned out to be leftover resin, which firmly adheres to the exterior of the model. It was observed that the residue was concentrated greatly in the middle of the design (Fig. 6A). The centralized white dot diminished in a gradient to the outer surfaces of the print. This surface contamination could not be washed of using an IPA bath or be blown off by a nitrogen gun. Withholding the IPA washing step is not advisable since leftover resin will adhere to the surface. Ironically, uncured resin can also accumulate in the

IPA tank, which settles on the print after washing. Sonification of prints in fresh IPA caused similar effects. This problem has major consequences for high-definition designs for biomedical applications. Surface contamination can barricade microstructures and therefore deteriorate their function. This would tamper with future fabrication steps such as microtransfer molding. To combat the white residue, prints were first dried and subsequently sonicated in IPA and acetone. This procedure was able to reduce large amounts of resin residue. However, two problems arose during this washing protocol: (i) not all powder was removed from the surface, and (ii) acetone is known to degrade polymer-based surfaces. Because the amount of residue depends on the resin, the Prusa resin was replaced by a Photocentric3D casting resin. This type of resin does not leave any residue behind, has a high quality and is popular in the industrial community. It was concluded that the resin cannot pollute the surface of 3D prints for microsieve production. Therefore, the type of resin

should be selected carefully to avoid such difficulties (Fig. 6B).

3D printing microsieves –

The 3D printing approach is a convenient additive manufacturing technique to fabricate biomedical devices in a quick and easy manner. This research explored the possibility of employing masked-stereolithography for high-definition microstructures. Virtual models of microsieves with square pores were generated as CAD files. The side length of each square was equal to a multiplicative discrete interval starting from 47 μm (max. length 470 μm). This discrete sequence of border dimensions has been appointed to the microsieve design because of the intrinsic mechanisms in masked-stereolithography. The spatial control of UV illumination within the resin tank is regulated by a LCD photomask. A series of two-dimensional projections is patterned by activation/deactivation of translucent pixels in the mask. The stacking of all projections results in a three-dimensional object. A major limiting factor in

masked-stereolithography resolution is the minimal pixel size. The fabrication of prototypes with a sub-pixel resolution cannot be achieved using this 3D printing technique. The Prusa SL1 3D printer has a high-resolution 5.5” display containing 2560 x 1440 pixels. Consequently, this results in 0.047 mm/pixel (XY-length) which is theoretically the smallest area that can be illuminated by UV light. The actual printing resolution was tested by fabricating a microsieve with a pore gradient ranging from 47 μm to 470 μm in side lengths. The optical microscope revealed that all pores became circular instead of square shaped. This is most likely due to diffraction of UV waves. It was noticed that closed pore formation starts around 329 μm x 329 μm . Fully open pores occur when the dimensions were set to be 470 μm x 470 μm , however the majority of pores were clogged (Fig 7A). Thus, further investigation was conducted using the 470 μm resolution. A second microsieve model was designed containing only an array of 470 μm pores. The majority of pores opened entirely, but their pore size varied greatly in each

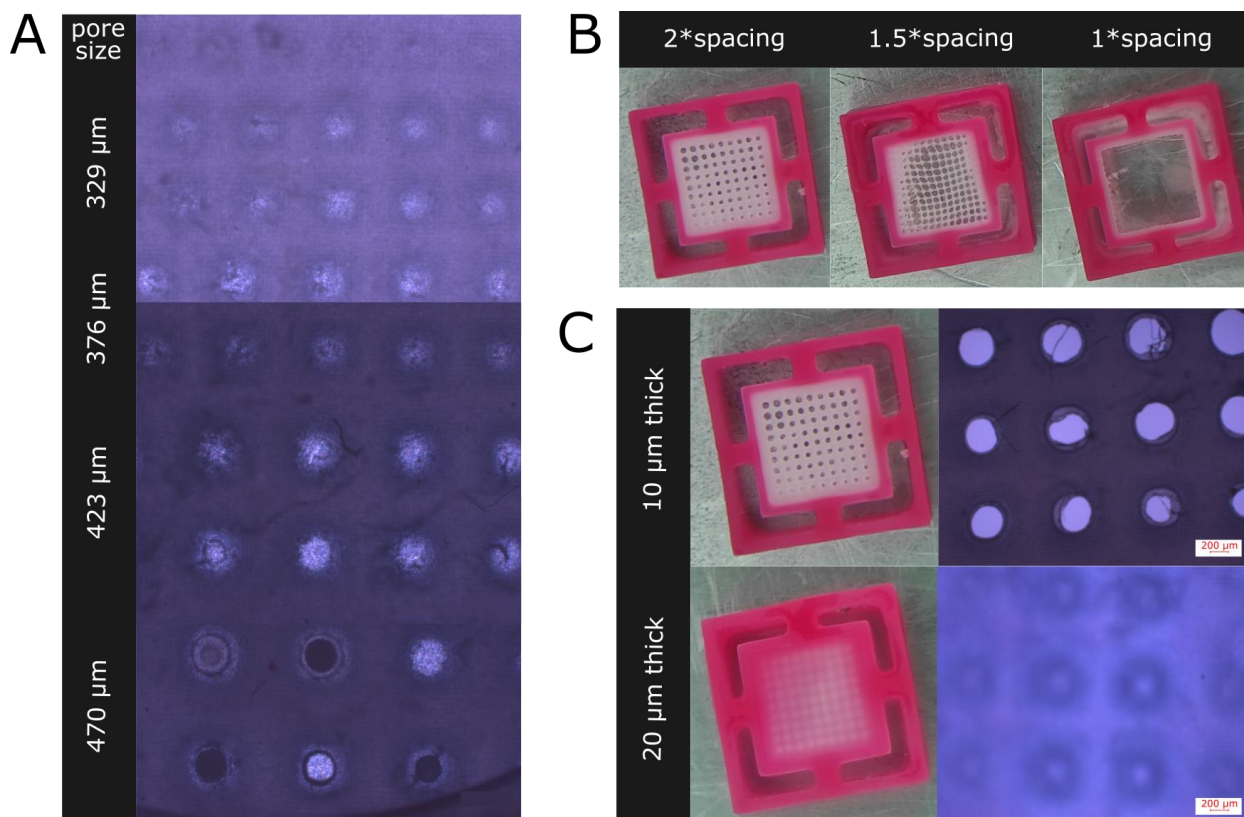


Figure 7: Pore formation in 3D-printed microsieves. (A) A gradient of pore sizes revealing closed, clogged and open pore formation. (B) The effect of pore spacing on the microsieve stability. (369 μm pore diameter) (C) The effect of pore wall thickness on pore formation.

model. The average pore size was estimated to be around 369 μm in diameter. Additionally, both the spacing (the distance between the middle points of two adjacent structures) between pores, and the pore wall thickness were examined at this resolution. As established previously, a spacing equal to two times the pore size resulted in a stable film with fully developed pores. However, reducing this spacing equal to or below 1.5 times the pore size made the microsieve film highly unstable and easy to rupture (Fig. 7B). A lower degree of spacing between apertures in a thin film is detrimental for the mechanical strength of the microsieve. The pore wall thickness is determined by the voxel depth. A voxel is similar to a pixel, but a third dimension is added. The minimum setting the 3D printer allows, is a thickness of 0.01 mm. Doubling the thickness results in clogged pores, thus making the former dimension more fitting (Fig. 7C).

In theory, square pore sizes of 47 μm x 47 μm should be possible if all conditions are met. The final resolution of physical 3D prints is dependent on multiple factors; like the 3D printing technique, the condition of the LCD photomask, the running-time of the LED array, the resin tank transparency, a correct calibration of the equipment, and so forth. Common problems regarding resin types are resin shelf life expiration, poorly mixing of resin constituents before use, and incompatibility of resin with the 3D printer. The intended ratio of the chemical composition of resin (monomers, oligomers, and photoactive agents) can diverge greatly if not mixed properly. Precipitation within the resin causes the elements to separate, therefore decreasing the chance of acquiring the intended resolution. Incompatibility between resin and 3D printer occurs if the recommended wavelength, light source power or resolution does not match. Next, the LCD photomasks degrades gradually because their pixels transform into a fixed open or closed state upon sufficient UV exposure. Apart from definitive fixation, pixels also tend to lose their opaqueness over time. These irregularities cause the seeping of UV light in locations where resin isn't supposed to solidify. The LED array experiences similar difficulties. Components tend to lose efficiency or break down entirely, especially during frequent usage of the device. Next, the calibration between the resin tank and building platform is performed manually, which leaves room for errors. Incorrect calibration affects 3D prints

negatively due to poor alignment of the inner (LED array, LCD photomask) and outer mechanics (resin bath, building platform). These errors are more apparent in structures with features close to the minimal printing resolution. Moreover, the transparent fluorinated ethylene propylene (FEP) film, which separates the resin from the LCD photomask, becomes more opaque after each print. This obscuration results in UV light diffraction, therefore affecting areas within the resin that were not meant to be illuminated. Also, prints are subjected to large mechanical stresses due to separation forces. An upward movement of the building platform sucks a new batch of viscous resin between the FEP film and newly cured print layers. The mechanical forces of the building platform must overcome the separating forces in order to break free from the resin tank. Consequently, microstructures can be distorted or destroyed if the necessary force is too strong.

Apart from mechanical considerations, voxel depth, overcuring depth and initial/general exposure times are printing process parameters which affect the resolution. These parameters should be set correctly, depending on the resin- and 3D printing type. A change of 3D printing technique could counteract the resolution and separation force problem. Recently, a modified version of stereolithography has emerged: continuous liquid interface production (51). Herein, a 'dead zone' of oxygen prevents resin solidification, thereby leaving liquid space in the order of tens of micrometers between the print and resin bath surface. As a consequence, separation forces cannot damage the print but provide suction to constantly resupply the building area with reactive resin components. Moreover, slicing artifacts are avoided because CLIP is a continuous approach. Tumbleston *et al.* has proven that an exceptional resolution can be achieved by making micropaddles with stems 50 μm in diameter (52). The introduction of an oxygen-permeable zone has many advantages over traditional stereolithography. The production of microfluidic systems could be eased by use of CLIP 3D printing technology. However, this type of 3D printer can cost up to 25k/year, which is roughly 10 times the price for a fully-owned SL1 MSLA printer.

Microtransfer molding -

The pattern transfer from 3D printed microsieves into a SU-8 photoresist film can be achieved by microtransfer molding. As a result, an identical microsieve can be created in a different, more suitable material. It is important to note that PDMS curing appeared to be inhibited by compounds in the print. The elastomeric material does not fully cure, therefore remains sticky and difficult to remove. Naturally, this phenomenon resulted in loss of resolution or even worse, the loss of the complete device. Unreacted monomers and oligomers of acrylate-based resin could quench PDMS polymerization. This left residual material behind both on the mold and microsieve 3D print. A way to combat this was by introducing methacrylate components to the mixture (53). Such

monomers and oligomers have no effect on PDMS curing. However, the Photocentric3D casting resin used during experiments does contain methacrylate elements but polymerization remains partially inhibited. The ratio acrylates/ methacrylates could be too high to enable proper curing. For that reason, surface treatment of the 3D print was required. A single coat of acrylic lacquer proved to be beneficial for PDMS curing, since molds became firm, non-adhesive and easy to peel off. During this treatment, highly-reactive acrylate anion groups are covered up by more stable acrylic acids. The latter compound contains an alcohol group at the end of its tail, instead of an anionic charge as seen in the former element. By means of separating the reactive groups from the PDMS mixture, successful curing is attained. A change in pore width by means

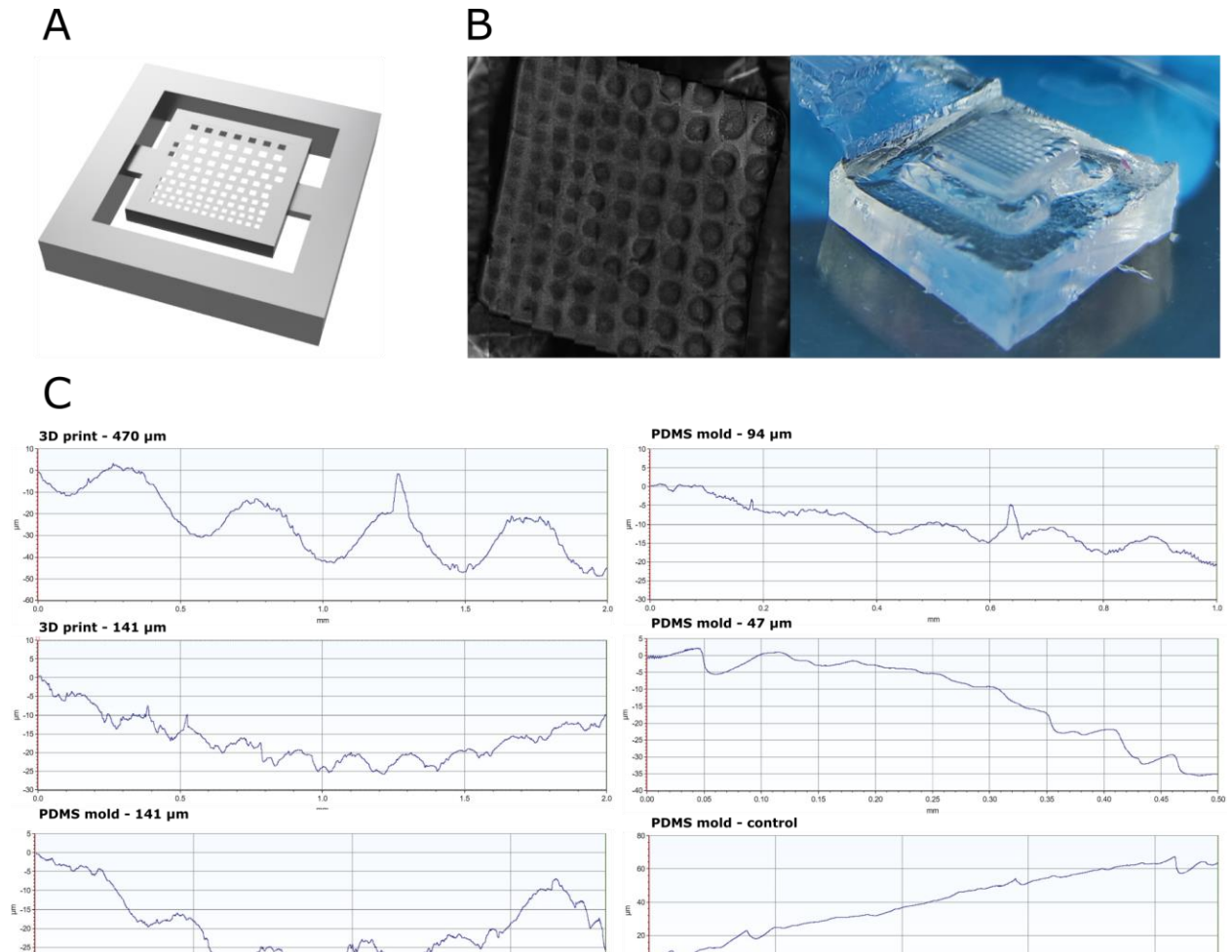


Figure 8: Topology of 3D prints and PDMS molds. (A) CAD file of microsieve gradient $470 \mu\text{m}^2$ to $235 \mu\text{m}^2$. (B) Visual by confocal microscope of hill-like structures in a PDMS mold gradient of $470 \mu\text{m}$ to $235 \mu\text{m}$ resolution. (B) A surface profilometer examined the topology of 3D prints with a $470 \mu\text{m}$ resolution (average hill width = $461 \mu\text{m}$), a $141 \mu\text{m}$ resolution (average = $153 \mu\text{m}$); and of PDMS molds of microsieves with the resolutions $141 \mu\text{m}$ (average = $241 \mu\text{m}$), $94 \mu\text{m}$ (average = $135 \mu\text{m}$), $47 \mu\text{m}$ (average = $43.7 \mu\text{m}$) and a control (average = $43.6 \mu\text{m}$)

of surface coating can be derived from measuring the width of PDMS pillars. The identical geometries are replicated after proper PDMS curing.

In the following experiments, the PDMS molds will be investigated. Microtransfer patterning requires an inverted pattern: in this case an array of pillars. The first PDMS mold was made from a 470 μm resolution microsieve print due to its fully opened pores. Later PDMS molds revealed that pore formation could still be accomplished from microsieves that obtained smaller but clogged pores. This suggest that the middle parts of closed pores were not as thick as its outer parts. The clogging was most likely created by UV light diffraction; less light had reached the inner part

compared to the pore edges, but was sufficient to solidify a thin layer. PDMS molds of microsieves with pore size gradients were created to establish the limit of pillar formation. A CAD file was generated in which the first gradient exhibits a range from 470 μm to 235 μm square pores (Fig. 8A). After molding, the bumps on the PDMS surface could be seen by the naked eye. Confocal microscopy revealed the existence of hill-like structures instead of pillars (Fig. 8B). Thus, this process created hills with a low aspect ratio at every pore size, instead of sharp-edged pillars as typically seen with photolithography. Using a surface profilometer on the resulting PDMS cast (Fig. 8C), a 3D microsieve print with 470 x 470 μm pores was investigated and a clear hole-like pattern was

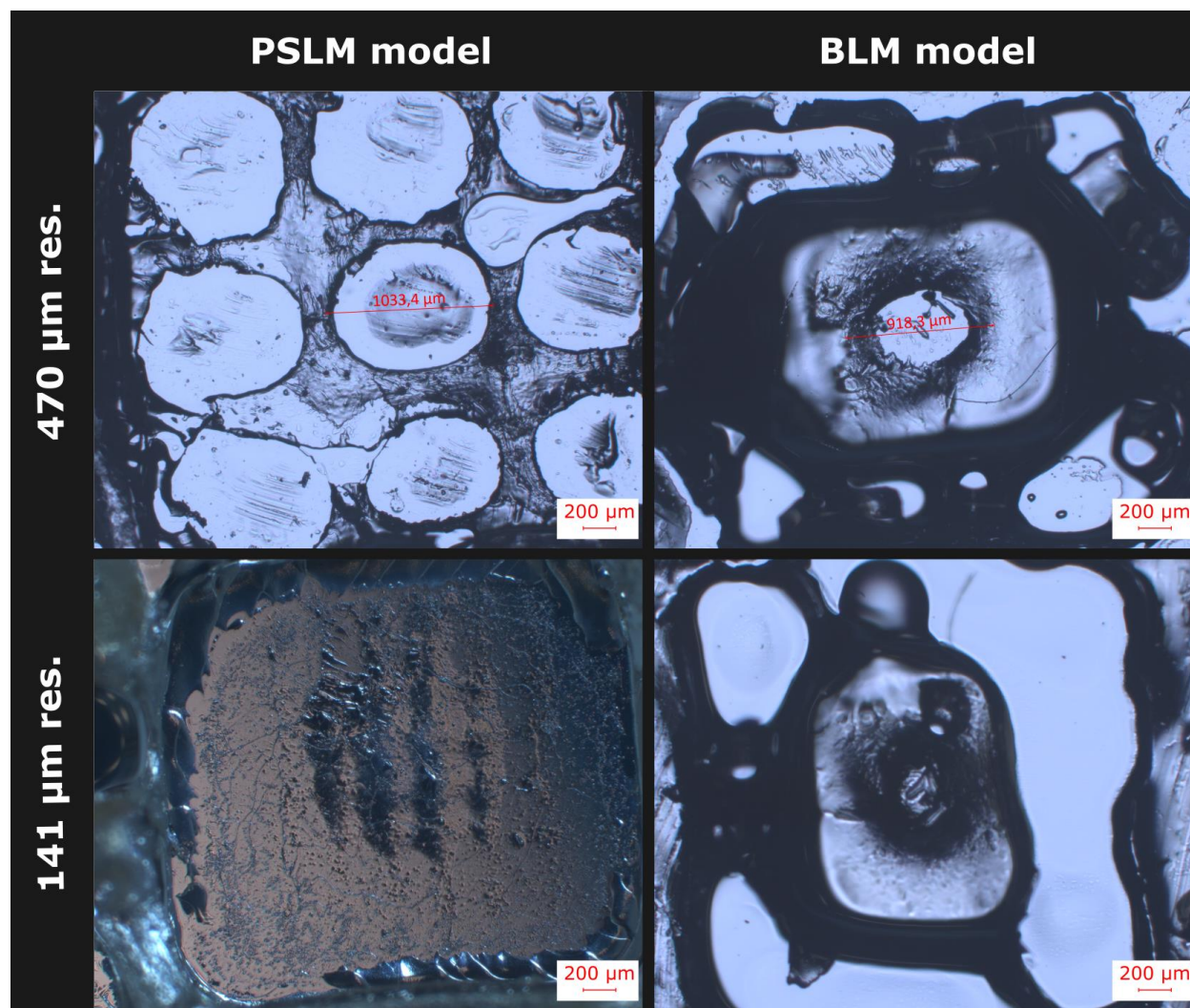


Figure 9: Pore pattern transfer to a SU-8 photoresist film. Microsieve masters with a 470 μm and 141 μm resolution were replicated by micromolding transfer for a pore-spanning lipid membrane model and black lipid membrane model. PSLM: pore-spanning lipid membrane; BLM: Black lipid membrane.

shown. A similar pattern was seen in 141 x 141 μm pore 3D prints, however the hills in the PDMS mold tended to become overshadowed by the surface roughness; this mold exhibited a warped surface with noisy hills. The hills become less apparent in 94 x 94 μm molds, but still hold a resemblance to the desired design. Lastly, 47 x 47 μm PDMS molds become unreliable because the pattern is lost by the surface roughness. However, the hill-like motif still seems to be slightly present when compared to a flat PDMS surface, which was molded by a 3D printed film. This indicates that the surface is affected by the 3D print design, however the resolution was insufficient to create reliable patterns. The distorted surface was a direct consequence of the resolution of both the resin and 3D printer. PDMS will perfectly replicate these imperfections of the surface, which will ultimately affect the end product.

Subsequently, the confirmation of hill-like structures in the PDMS stamps led to the possibility of pattern transfer. UV illumination of a negative photoresist within the PDMS stamp would result in an identical replication of the microsieve master. The first mold was made from a 470 μm x 470 μm 3D print; it was able to develop open pores inside the SU-8 film. However, the pore sizes had doubled to a diameter of approximately 1 mm (Fig. 9). A topological analysis had previously established the existence non-uniform sizes of hills on a warped PDMS surface. A correct microtransfer molding procedure requires a planar surface with microstructures equal in height. In this study, the PDMS molds have to be mechanically compressed against a glass substrate. The microstructures have to contact the substrate surface to develop pores, but irregularities in the surface prevented this from happening without external pressure. The PDMS molds are an elastomeric material, which tends to increase the surface contact area if compressed heavily. Consequently, the pore diameters within the photoresist become significantly bigger than the PDMS mold hills. Further, stamps with a smaller 141 μm resolution remained closed, even after applying a high degree of compression. This mold was only able to produce small dents in the photoresist film. However, only a small portion of hills made an imprint in the surface. These pores were closed and connected to each other, which is far from ideal. Open pores are a desirable feature to

access both sides of the lipid membrane within a microfluidic device. To test the usability of this procedure for black lipid membrane models, the same methods were applied. The difference is that the array of pores in the 3D print are replaced by one singular hole in the middle of the design. This resulted in similar outcomes; a pore diameter around 1 mm and fabrication of closed pores when going below a 470 μm resolution.

Contact lithography

Positive photoresist film –

A second method to easily fabricate microsieves was designed and tested. A photomask was directly placed on a positive- or negative photoresist. Depending on the photoresist, either monomers polymerized or polymers broke down when exposed to UV illumination. The photomask shielded sections that were not meant to interact with UV waves. First, a dry film photoresist was thermally attached to a glass slide. Next, a TEM grid containing 125 μm square pores served as the photomask. Different UV exposure times were analyzed to study the degree of photopositive resist cross-linking: 15 s, 20 s and 30 s (Fig. 10). The USB camera revealed that pore arrays were formed in all positive photoresist films. However, no high-definition pore formation was observed after any of the exposure times. A time interval of 30 s has the closest approximation of pore-like features, but the array is highly inconsistent and disrupted in many places. Even if a higher resolution is achieved, proper microsieve patterning would become impossible for photomasks with smaller features. The UV emitter in this experiment does not guarantee that all light travels perpendicular with the photomask. Furthermore, the thickness of the photoresist film could be responsible for the poor performance. These PCB films possess a thickness of around 200 μm , which causes a high degree of light diffraction. This will drastically lower the patterning resolution in the microsieve design. As mentioned before, the minimum feature size for contact lithography is highly dependent on film thickness. Travelling of UV light through various media (air, glass, photoresist, etc.) with different refractive indices will cause the waves to diverge from a straight path. Additionally, a diffraction grating pattern would be created because the TEM grid consist of a series of holes. This phenomenon

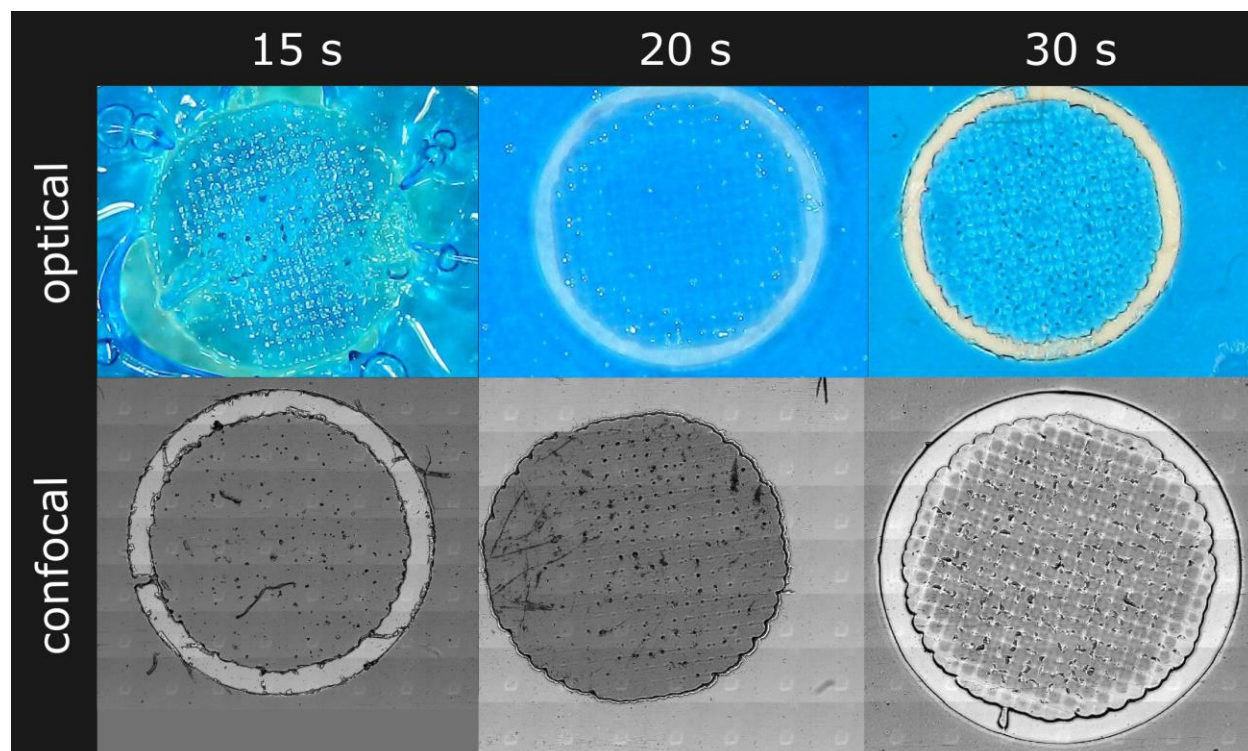


Figure 10: Patterning of TEM grid in positive photoresist. UV exposure times of 15 s, 20 s, and 30 s were examined by patterning a 125 μm resolution TEM grid in a positive photoresist. The results are visualized by both optical and confocal microscopy.

interferes with the pattern transfer since UV waves propagate in various angles when passing through the apertures. This results in unspecific UV exposure of the photopositive film, therefore crosslinking monomers in places where solidification is undesirable. A way to combat these problems is by working with thinner photoresists and to use a collimated light source during the exposure step. The change in direction of waves becomes more less prominent if light travels shorter distances through the photoresist. A thick layer of resist will be more affected by non-specific UV exposure because the waves reach further distances from their origin opposed to thinner films. Altering wavelengths is another method to increase resolution in the field of optics. However, UV-sensitive materials have fixed wavelengths in which polymerization occurs optimally. This means that the wavelengths usually cannot be adjusted to achieve greater high-definition structures.

Negative photoresist film –

The thickness of the film should be reduced to maximize the MFS during contact lithography. Replacing a dry film with a liquid photoresist could

provide a solution. This difference in state of matter allows the photoresist to be spread thinly by a thin-coating process. During the two-step fabrication method experiments, a negative photoresist SU-8 was used because of its biocompatible character and mechanical strength. This type of photoresist is a liquid mixture of monomers and photoactive agents, which solidify when exposed to UV light. Thus, the liquidity can be taken advantage of by spin-coating the material over a glass substrate. This series of SU-8 (2005) can achieve a thickness of 8 to 10 micrometer, which is a considerable difference compared to the dry photoresist film. Again, a TEM grid containing 125 μm square pores was pressed against the substrate surface and subsequently exposed to UV waves. A much better result was obtained opposed to the dry film, therefore enforcing the theory about minimizing photoresist thickness for high-resolution microstructures. Clear cut-edge pillars of similar height were created with almost no artifacts in the design (Fig. 11A). Using an optical microscope, the pillar width was estimated to be approximately 210 μm . Therefore, this resulted in a 70% increase when compared to the actual aperture size. Next, a

A



B

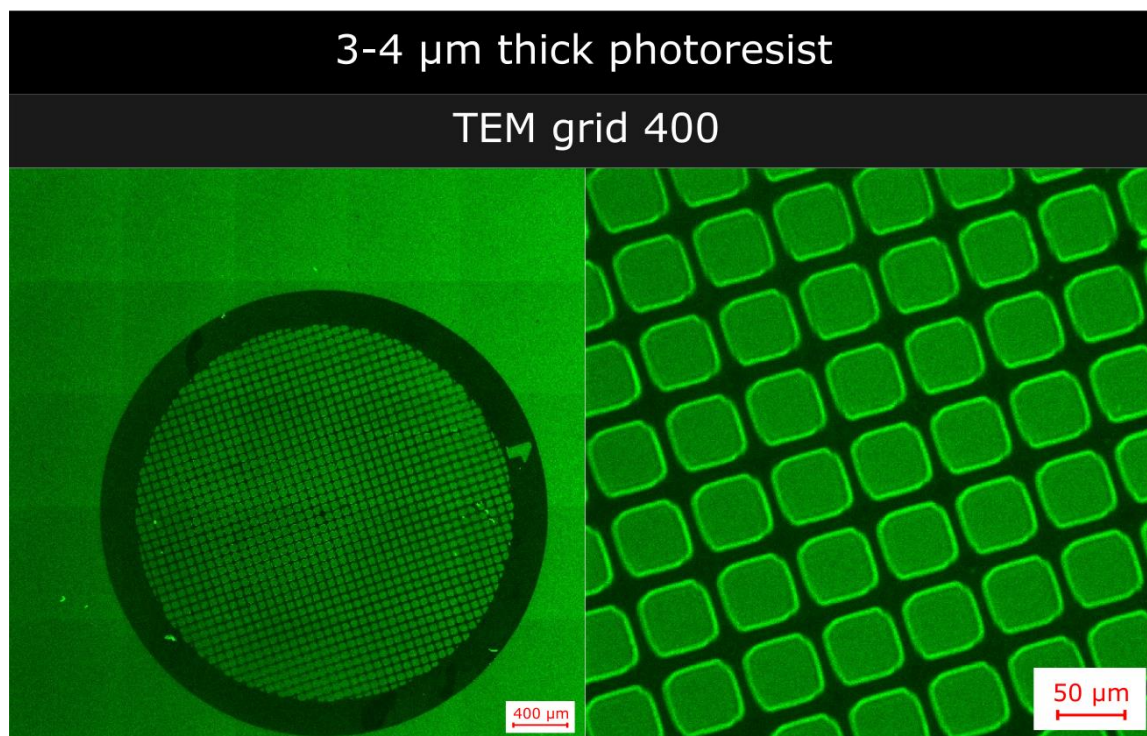


Figure 11: Patterning of a TEM grid in spin-coated SU-8. (A) A TEM grid 200/400 (125 μm) was patterned in 8-10 μm SU-8. Visualized by optical microscopy. (B) A TEM grid 400 was patterned in 3-4 μm SU-8. Visualized by confocal microscopy

TEM grid containing 62 μm square pores was applied directly to the photoresist. After illumination, a vague pattern of the grid was

imprinted in SU-8. On average, the pillar width of this design was measured to be about 97 μm . When compared to the photomask apertures, a 56%

increase in pore size was observed. Additionally, the confocal microscope revealed that pores were partially closed. No pattern could be distinguished by fluorescence imaging, but a pattern could be seen by the naked eye. This means that a thin layer of SU-8 remained on the glass substrate, thereby creating a half-open pore. The exposure time could have been too high. Also, the light diffraction phenomenon plays a major role in high-resolution fabrication. The increase in pore size, the vagueness of smaller patterns and the occurrence of partially closed pores is probably due to diffraction. A higher resolution was achieved by thinning the SU-8 coat further down to 3-4 μm . Visualization by confocal microscopy revealed pillars with average widths around 55 μm (Fig. 11B). Although this method achieves high-resolution microstructures, the used photoresist had a negative character. Consequently, the resist became insoluble in locations which were exposed to UV illumination. Thus, a negative photoresist results in pillars instead of pore arrays. Ideally, a liquid positive photoresist with a biocompatible character or the capacity for non-toxic surface modifications would be thin-coated on a sacrificial layer substrate. A possible contender could be the MicropositTM SPRTM 220 series, because this positive photoresist can be spin-coated to a range between 1-10 μm . The photoresist has a biocompatible character and is therefore commonly used for microelectromechanical systems (MEMS). Moreover, the surface is modifiable, which is advantageous for transmembrane protein-anchoring or biocompatibility enhancement. Contact lithography on a 1 μm thick positive photoresist film could eventually result in an easy-to-fabricate microsieve for PSLM applications.

CONCLUSION

In summary, this work tested two novel prototyping methods for PSLM microsieve fabrication. Regarding the two-step fabrication method, it was shown that the resin type is an important part during additive manufacturing of microstructures. A residue-free surface is essential for PDMS molding to obtain optimal results. It was

further proven that the MSLA machinery had trouble creating pores with predetermined diameters below 470 μm . Further, it was impossible to diverge from the established pore wall thickness and pores spacing. Various mechanical and theoretical reasons were given for this lack of resolution. Moreover, surface coating was required for proper PDMS curing, which could also influence the geometries. A poor pattern transfer was achieved because microtransfer molding is highly dependent on the quality of the master. A warped surface with an excessive noisy topology resulted in pores around 1 mm. It was concluded that a novel 3D printing technique should be tested instead of MSLA. As a suggestion, CLIP printing could reach resolutions far beyond the standard 3D printer. The second novel prototyping method involved the simplification of contact lithography to reduce costs and labor, while retaining resolution. It was found that dry films were no good match with contact lithography. The minimum feature size is heavily dependent on photoresist thickness. Therefore, a liquid photoresist which can be spin-coated was ideal. SU-8 substrates proved that great resolution was achievable with thin layers resist. Square pillars with 210 μm side lengths were patterned in 8-10 μm . Next, square pillars with 55 μm in side length were achieved by reducing the film thickness with 5-6 μm . We hypothesize that thinner photoresist films with higher-definition photomasks would result in better resolutions. It must be noted that the negative SU-8 photoresist should be replaced by a liquid positive photoresist. The MicropositTM SPRTM 220 series is a potential candidate for further research, since it is commonly seen as SU-8's counterpart. In conclusion, the two-step fabrication method requires the most work to obtain the required resolutions for PSLM. A change of technique could set the way for reliable, rapid prototyping for PSLM models. In contrast, the simplified contact lithography seems the most promising. The better resolution, faster procedure and lower costs makes this technique the most attractive for microsieve fabrication.

REFERENCES

1. Sezgin E, Levental I, Mayor S, Eggeling C. The mystery of membrane organization: composition, regulation and roles of lipid rafts. *Nat Rev Mol Cell Biol.* 2017;18(6):361-74.
2. R. E, J-M. R. *The Biophysics of Cell Membranes: Biological Consequences*: Springer; 2017.
3. Harayama T, Riezman H. Understanding the diversity of membrane lipid composition. *Nat Rev Mol Cell Biol.* 2018;19(5):281-96.
4. Sachse R, Dondapati SK, Fenz SF, Schmidt T, Kubick S. Membrane protein synthesis in cell-free systems: from biomimetic systems to bio-membranes. *FEBS Lett.* 2014;588(17):2774-81.
5. Lukas BK. *Cell Membranes*. S. S, M. T, W. N, W. S, editors: Garland Science; 2016.
6. Casares D, Escriba PV, Rossello CA. Membrane Lipid Composition: Effect on Membrane and Organelle Structure, Function and Compartmentalization and Therapeutic Avenues. *Int J Mol Sci.* 2019;20(9).
7. Kalappurakkal JM, Sil P, Mayor S. Toward a new picture of the living plasma membrane. *Protein Sci.* 2020;29(6):1355-65.
8. Raote I, Malhotra V. Protein transport by vesicles and tunnels. *J Cell Biol.* 2019;218(3):737-9.
9. Schwenk RW, Holloway GP, Luiken JJ, Bonen A, Glatz JF. Fatty acid transport across the cell membrane: regulation by fatty acid transporters. *Prostaglandins Leukot Essent Fatty Acids.* 2010;82(4-6):149-54.
10. Juste YR, Cuervo AM. Analysis of Chaperone-Mediated Autophagy. *Methods Mol Biol.* 2019;1880:703-27.
11. Rafeeq MM, Murad HAS. Cystic fibrosis: current therapeutic targets and future approaches. *J Transl Med.* 2017;15(1):84.
12. Gonzalez R, Hamblin MH, Lee JP. Neural Stem Cell Transplantation and CNS Diseases. *CNS Neurol Disord Drug Targets.* 2016;15(8):881-6.
13. Cundy T. Paget's disease of bone. *Metabolism.* 2018;80:5-14.
14. Dong YH, Fu DG. Autoimmune thyroid disease: mechanism, genetics and current knowledge. *Eur Rev Med Pharmacol Sci.* 2014;18(23):3611-8.
15. Wallace MA. Anatomy and physiology of the kidney. *AORN J.* 1998;68(5):800, 3-16, 19-20; quiz 21-4.
16. Riley RS, June CH, Langer R, Mitchell MJ. Delivery technologies for cancer immunotherapy. *Nat Rev Drug Discov.* 2019;18(3):175-96.
17. Kurniawan J., Ventrici de Souza J., A. D. Preparation and Characterization of Solid-Supported Lipid Bilayers Formed by Langmuir–Blodgett Deposition: A Tutorial. *Langmuir.* 2018.
18. A. J, Jackman, Cho N-J. Supported Lipid Bilayer Formation: Beyond Vesicle Fusion. *Langmuir.* 2020.
19. Kiessling V, Yang ST, Tamm LK. Supported lipid bilayers as models for studying membrane domains. *Curr Top Membr.* 2015;75:1-23.
20. Spindler S, Sibold J, Gholami Mahmoodabadi R, Steinem C, Sandoghdar V. High-Speed Microscopy of Diffusion in Pore-Spanning Lipid Membranes. *Nano Lett.* 2018;18(8):5262-71.
21. Glazier R, Salaita K. Supported lipid bilayer platforms to probe cell mechanobiology. *Biochim Biophys Acta Biomembr.* 2017;1859(9 Pt A):1465-82.
22. Khan MS, Dosoky NS, Williams JD. Engineering lipid bilayer membranes for protein studies. *Int J Mol Sci.* 2013;14(11):21561-97.
23. Weiss K, Enderlein J. Lipid diffusion within black lipid membranes measured with dual-focus fluorescence correlation spectroscopy. *Chemphyschem.* 2012;13(4):990-1000.
24. Heo P, Ramakrishnan S, Coleman J, Rothman JE, Fleury JB, Pincet F. Highly Reproducible Physiological Asymmetric Membrane with Freely Diffusing Embedded Proteins in a 3D-Printed Microfluidic Setup. *Small.* 2019;15(21):e1900725.
25. Dugger ME, Baker CA. Automated formation of black lipid membranes within a microfluidic device via confocal fluorescence feedback-controlled hydrostatic pressure manipulations. *Anal Bioanal Chem.* 2019;411(19):4605-14.
26. Janshoff A, Steinem C. Mechanics of lipid bilayers: What do we learn from pore-spanning membranes? *Biochim Biophys Acta.* 2015;1853(11 Pt B):2977-83.
27. Neubacher H, Mey I, Carnarius C, Lazzara TD, Steinem C. Permeabilization assay for antimicrobial peptides based on pore-spanning lipid membranes on nanoporous alumina. *Langmuir.* 2014;30(16):4767-74.
28. Mey I, Stephan M, Schmitt EK, Muller MM, Ben Amar M, Steinem C, et al. Local membrane mechanics of pore-spanning bilayers. *J Am Chem Soc.* 2009;131(20):7031-9.
29. Van Rijn C, Elwenspoek M. Micro filtration membrane sieve with silicon micro machining for industrial and biomedical applications. *Aquamarijn Microfiltration BV.* 1995.
30. Elwenspoek M, al. e. *Silicon Micromachining*. Berlin Heidelberg: Springer-Verlag; 2001.
31. Qin D, Xia Y, Whitesides GM. Soft lithography for micro- and nanoscale patterning. *Nat Protoc.* 2010;5(3):491-502.
32. Melchels FP, Feijen J, Grijpma DW. A review on stereolithography and its applications in biomedical engineering. *Biomaterials.* 2010;31(24):6121-30.
33. Pan Y, Zhou C, Chan Y. A Fast Mask Projection Stereolithography Process for Fabricating Digital Models in Minutes. *Journal of Manufacturing Science and Engineering.* 2012;134.
34. Gong H, Bickham BP, Woolley AT, Nordin GP. Custom 3D printer and resin for 18 μm x 20 μm microfluidic flow channels. *Lab Chip.* 2017;17(17):2899-909.
35. Potgieter J, Zyzalo JR, Diegel O, Xu WL. Layer Curing for Masked Projection Stereolithography: the effects of varying irradiance distributions. *15th International Conference on Mechatronics and Machine Vision in Practice.* 2008.

36. Kuo AP, Bhattacharjee N, Lee YS, Castro K, Kim YT, Folch A. High-Precision Stereolithography of Biomicrofluidic Devices. *Adv Mater Technol.* 2019;4(6).
37. Razavi Bazaz S, Rouhi O, Raoufi MA, Ejeian F, Asadnia M, Jin D, et al. 3D Printing of Inertial Microfluidic Devices. *Sci Rep.* 2020;10(1):5929.
38. Urrios A, Parra-Cabrera C, Bhattacharjee N, Gonzalez-Suarez AM, Rigat-Brugarolas LG, Nallapatti U, et al. 3D-printing of transparent bio-microfluidic devices in PEG-DA. *Lab Chip.* 2016;16(12):2287-94.
39. Kim AA, Kustanovich K, Baratian D, Ainla A, Shaali M, Jeffries GDM, et al. SU-8 free-standing microfluidic probes. *Biomicrofluidics.* 2017;11(1):014112.
40. Bronder AM, Bieker A, Elter S, Etzkorn M, Haussinger D, Oesterhelt F. Oriented Membrane Protein Reconstitution into Tethered Lipid Membranes for AFM Force Spectroscopy. *Biophys J.* 2016;111(9):1925-34.
41. Zhou ZF, Huang QA. Comprehensive Simulations for Ultraviolet Lithography Process of Thick SU-8 Photoresist. *Micromachines (Basel).* 2018;9(7).
42. Cavallini M, Murgia M, Biscarini F. Direct patterning of tris- 8-hydroxyquinoline-aluminum III thin film at submicron scale by modified micro-transfer molding. *Elsevier Materials science and Engineering.* 2002.
43. Li Q, Peer A, Cho IH, Biswas R, Kim J. Replica molding-based nanopatterning of tribocharge on elastomer with application to electrohydrodynamic nanolithography. *Nat Commun.* 2018;9(1):974.
44. Zhao X-M, Xia Y, Whitesides GM. Fabrication of Three-Dimensional Micro-Structures: Microtransfer Molding. *Adv Mater.* 1996.
45. Halldorsson S, Lucumi E, Gomez-Sjoberg R, Fleming RMT. Advantages and challenges of microfluidic cell culture in polydimethylsiloxane devices. *Biosens Bioelectron.* 2015;63:218-31.
46. Torino S., Corrado B., Iodice M., G. C. PDMS-Based Microfluidic Devices for Cell Culture. Institute for Microelectronics and Microsystems. 2018.
47. Thompson LF. *An Introduction to Lithography.* ACS Symposium Series: American Chemical Society. 1983.
48. Francioso L., P. S. Top-down contact lithography fabrication of a TiO₂ nanowire array over a SiO₂ mesa. Institute of Physics Publishing. 2006.
49. R. W. *Nanoelectronics and Information Technology: Advanced Electronic Materials and Novel Devices.* 3 ed 2012.
50. J. LH. *Principles of Lithography.* Fourth ed: Spie Press Book; 2019.
51. Qin L., Fei Y., Hua X., L. D. Oxygen-controlled bottom-up mask-projection stereolithography for ceramic 3D printing. *Ceramics International.* 2017.
52. Tumbleston J. R., Shirvanyants D., M. DJ. Continuous liquid interface production of 3D objects. *Sciencemag.* 2015.
53. Bazaz R. S., Kashaninejad N., M. WE. Rapid Softlithography Using 3D-Printed Molds. *Advanced Materials Technologies.* 2019.

Acknowledgements – TF acknowledges the IMO-IMEC for his Master internship. Prof. dr. ir. R. Thoelen is thanked for providing access to his facilities. Prof. dr. J. Hendrix (Biomed, University of Hasselt, Diepenbeek) is gratefully acknowledged for providing access to confocal microscopy. Research was funded by UHasselT.

Author contributions – TF, TV, SD and RT conceived and designed the research. TF performed experiments and data analysis. TV and SD provided assistance with optical/confocal microscopy and surface profilometry. TF wrote the paper. All authors carefully edited the manuscript.